The Astrophysical Journal, 966:109 (12pp), 2024 May 1 https://doi.org/10.3847/1538-4357/ad35b9

Mining the GALAH Data. I. Study of Five Super Lithium-rich Metal-poor Giants

Antony Susmitha, Anohita Mallick, and Bacham E. Reddy
Indian Institute of Astrophysics, II Block, Koramangala, Bengaluru, Karnataka, 560034 India
Received 2023 December 19; revised 2024 March 18; accepted 2024 March 18; published 2024 April 29

Abstract

The presence of a large amount of Li in giants is still a mystery. Most of the super Li-rich (SLR) giants reported in recent studies are in the solar metallicity regime. Here, we study the five metal-poor SLRs from the Galactic Archeology with HERMES Data Release 3, with their [Fe/H] ranging from −1.35 to −2.38 with lithium abundance of $A(\mathrm{Li}) \geqslant 3.4$ dex. The asteroseismic analysis reveals that none are on the red giant branch. The average period spacing (ΔP) values indicate giants are in the core He-burning phase. All of them are low-mass giants ($M < 1.5\,M_{\odot}$). Their location in the Hertzsprung–Russell diagram suggests one of them is in the red clump (RC) phase, and interestingly, the other four are much brighter and coincide with the early asymptotic giant branch phase. The analysis of the abundance reveals that C, O, Na, Ba, and Eu are normal in giants of respective metallicities and evolutionary phases. Further, we did not find any strong evidence of the presence of dust in the form of infrared excess or binarity from the available radial velocity data. We discuss a few scenarios for the existence of SLRs at higher luminosity, including past merger events. Our findings will help in understanding the production and evolution of Li among giants, in particular, during the RC phase and the post-RC phase.

Unified Astronomy Thesaurus concepts: Chemically peculiar stars (226); Giant stars (655); Lithium stars (927)

1. Introduction

Lithium is expected to deplete as stars evolve off the main sequence and climb up toward the tip of the red giant branch (RGB). Models predict Li abundance ($A(\mathrm{Li}) = \log N(\mathrm{Li})/\log N(\mathrm{H}) + 12$), post first dredge-up, not more than $A(\mathrm{Li}) = 1.5$–1.8 dex, depending on the mass (Iben 1967; Gratton et al. 2000; Lind et al. 2009b). A few of them have A(Li) exceeding the initial abundance of the interstellar medium (ISM), $A(\mathrm{Li}) = 3.2$ dex (Knauth et al. 2003), with which stars have formed. The high A(Li) in red giants has been a puzzle for more than four decades since its discovery in 1982 (Luck 1982; Wallerstein & Sneden 1982).

In recent years, significant advances have been made in understanding the origin of high A(Li) in giants. This is mainly due to large data sets from spectroscopic surveys like the Large Sky Area Multi-Object Fiber Spectroscopic Telescope and Galactic Archeology with HERMES (GALAH) and time-resolved photometry from space missions like Kepler. A large number of spectra have helped increase Li-rich samples by many folds, and the asteroseismic data from the Kepler mission have helped resolve the stars' evolutionary phase in the Hertzsprung–Russell (H-R) diagram. These studies suggest that all the Li-rich giants are in the core He-burning phase of the red clump (RC) region (Deepak 2019; Singh et al. 2019). Kumar et al. (2020) demonstrated that giants ascending the RGB only deplete Li and reach A(Li) as low as −0.9 dex toward the tip of the RGB. Many studies have shown that high Li occurs during the He-flash episode, which terminates the further evolution of the RGB phase. These studies argued that the He flash is the only main stellar episode between the end of the RGB phase and the beginning of the RC phase. Hence, the He flash holds the key to the origin of high Li in RCs. In a novel study, Singh et al. (2021) showed that the A(Li) in RC giants and the gravity-mode period spacing (Πp) are correlated. In that, the giants with high A(Li), relatively younger RCs, have low Πp values compared to giants with normal A(Li), relatively older RCs. They concluded that A(Li) enrichment probably occurred within 2 Myr since the ignition of He began at the RGB tip. The study also demonstrated that Li-richness is a transient phenomenon. Further evidence was put forward by Mallick et al. (2023) in which they studied Li abundance in samples of low- ($\leqslant 2\,M_{\odot}$) and high-mass ($>2\,M_{\odot}$) giants. Interestingly, they found no Li-rich giants among high-mass stars, suggesting that He flash is the most likely cause of Li enrichment as high-mass giants are not expected to undergo He flash, but low-mass giants do. It is reasonable to believe that Li enrichment occurred during the He flash. However, it is not very clear how the Li produced in the interiors was brought to the surface, though a few mechanisms have been proposed (Cameron & Fowler 1971; Fekel & Balachandran 1993; Sackmann & Boothroyd 1999; Charbonnel & Balachandran 2000; Denissenkov & VandenBerg 2003; Kumar et al. 2011; Lattanzio et al. 2015). Most of the Li-rich giants in the recent literature are in the metal-rich regime, i.e., [Fe/H] $\geqslant -1.0$ dex.

Not many Li-rich giants have been found among metal-poor giants. Only a handful of stars have been detected in the metal-poor regime (Ruchti et al. 2011; Li et al. 2018; Casey et al. 2019), whose evolutionary phase was not explicitly constrained. The question is whether the mechanism that drives the Li enhancement in metal-rich giants is the same for the metal-poor giants. Increasing the Li-rich metal-poor giants and resolving their evolutionary phase may provide further constraints on Li production, the dredge-up process, and its evolution.

Here, we report the results on five super Li-rich (SLR) giants found while searching a sample of metal-poor giants in the GALAH Data Release 3 (DR3) survey for which asteroseismic data is available.

Table 1
Basic Data of the Five SLR Giants from GALAH DR3

Object Name	R.A. (hh:mm:ss)	Decl.	V_{mag}	A(Li) (dex)	$\log(L/L_{\odot})$	RV_{GALAH} (km s^{-1})	$RV_{GaiaDR3}$ (km s^{-1})
UCAC4 253-045343	$10^h25^m28.^s84$	$-39°26'01.''09$	12.6	3.74	3.01	171.3 ± 0.13	170.8 ± 0.24
UCAC4 099-098976	$23^h07^m10.^s10$	$-70°18'55.''61$	12.8	4.08	1.70	183.0 ± 0.31	182.3 ± 1.51
UCAC4 212-183136	$20^h29^m16.^s13$	$-47°41'51.''51$	13.8	4.23	2.71	5.9 ± 0.23	6.2 ± 1.53
UCAC4 308-077592	$14^h31^m09.^s66$	$-28°29'45.''42$	13.3	4.80	3.23	-115.7 ± 0.13	-115.0 ± 1.06
TYC 7262-250-1	$13^h09^m32.^s26$	$-37°09'17.''79$	11.5	4.54	3.00	30.7 ± 0.10	30.3 ± 0.34

2. Sample Selection

We utilized the recently released GALAH DR3 survey (Buder et al. 2021) to study the Li abundance in metal-poor giants. The GALAH survey employs the High Efficiency and Resolution Multi-Element Spectrograph (HERMES; Sheinis et al. 2015) mounted on the 3.9 m Anglo Australian Telescope (AAT). HERMES provides high-resolution ($R \sim$28,000) optical spectra in four wavelength windows (4713–4903 Å, 5648–5873 Å, 6478–6737 Å, and 7585-7887 Å) covering the spectral features of up to 30 elements, including Li. We used specific selection criteria provided in the GALAH catalog as bit flags to ensure the quality of the data and accuracy in stellar parameter estimation. These criteria include `flag_sp = 0`, `flag_fe_h = 0`, and `flag_Li_fe = 0`. Bit flag = "0" indicates that abundances are reliable and no problems were detected in determining the stellar parameters, and iron and Li abundances. Further, since we only focus on metal-poor giants, we applied the criteria $\log g < 3.0$ and $[Fe/H] \leqslant -1.0$, which resulted in a sample of 1038 metal-poor giant stars from the GALAH DR3 survey. Among the selected sample stars, we found five SLR giants with very high Li abundances, higher than the present ISM value (A(Li) ~3.2). We did not impose any other selection criteria to restrict the samples, such as mass or signal-to-noise ratio (S/N). The spectra of five giants were downloaded from the GALAH survey website for the analysis of the spectra and to search for additional peculiarities that might be present. The details of the five giants are provided in Table 1 and their location in the H-R diagram is shown in Figure 1. Note that Martell et al. (2021) listed all five giants as Li-rich giants in their catalog.

3. Stellar Parameters and Elemental Abundances

We found minor differences between the values by comparing the temperatures derived from photometric colors and those listed in the GALAH catalog. Since the Li abundance is derived from the resonant line at 6707 Å, which is very temperature sensitive, any variation in the temperature can lead to potential uncertainties in the values of Li abundance. To address this issue and ensure the reliability of the values adopted from the catalog data, we rederived the stellar parameters and elemental abundances by analyzing the spectra. We used version 12 of the spectral synthesis code TURBOSPECTRUM developed by Plez (2012) to derive abundances and stellar parameters. We used the stellar atmospheric models by Mészáros et al. (2012), in which the ATLAS9 and MARCS codes were modified with an updated H_2O line list and with a wide range of C and α-enhancements. We have used only carbon normal models as none of our stars exhibit enhancement in carbon. One-dimensional local thermodynamic equilibrium (LTE) is assumed for all the species. We applied the non-LTE corrections wherever they were available in the literature (see Table 3).

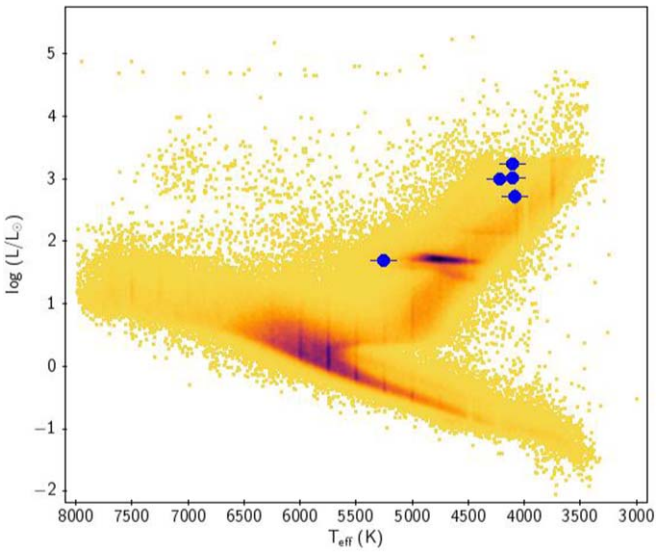

Figure 1. H-R diagram showing the five metal-poor SLRs along with stars in the background from the GALAH DR3 catalog (yellow points). Note the well-defined RGB, luminosity bump, and RC. One of the five SLRs is at the RC and the remaining four are at or close to the early AGB.

We adopted the solar abundances from Asplund et al. (2009). The line lists for atomic lines were assembled from the Vienna Atomic Line Database (Kupka et al. 1999). A hyperfine structure has been accounted for the transitions of elements Li, Ba, and Eu. For the molecular line lists, we used C2 data from the Kurucz database and CN data from Plez & Cohen (2005).

3.1. Stellar Parameters

We measured the equivalent width (EW) of unblended neutral and singly ionized Fe lines to derive the stellar parameters. EWs were measured by fitting Gaussian profiles to the features using the splot task in PyRAF.[1] We considered only those lines whose EW is less than 100 mÅ since they are on the linear part of the curve-of-growth and are relatively insensitive to the choice of microturbulence (Mucciarelli 2011). The uncertainties in the measurements were determined using the revised Cayrel formula (Cayrel 1988; Battaglia et al. 2008). We interpolated the models from the grid of atmospheric models provided by Mészáros et al. (2012) to obtain models of specific stellar parameters. The T_{eff} was derived by forcing the abundances of Fe I lines giving the same abundance irrespective of the line's lower excitation potential (LEP). We

[1] PYRAF is a product of the Space Telescope Science Institute, operated by AURA for NASA.

Table 2
Atmospheric Parameters of the Five SLR Giants Taken from the GALAH Catalog and Derived in This Study

Object Name	GALAH DR3				$T_{\rm eff}$ (V-K)	$T_{\rm eff}$ Gaia	This Study				
	$T_{\rm eff}$ (K)	log g (dex)	[Fe/H] (dex)	ξ_t (km s^{-1})	(K)	(K)	$T_{\rm eff}$ (K)	log g (dex)	[Fe/H] (dex)	ξ_t (km s^{-1})	$v \sin i$ (km s^{-1})
UCAC4 253-045343	4308 ± 90	1.06 ± 0.31	−1.26 ± 0.07	1.6	4025	4327	4100	1.00	−1.43 ± 0.14	1.4	6.0
UCAC4 099-098976	5263 ± 101	2.49 ± 0.22	−1.46 ± 0.12	1.1	5205	5375	5260	2.49	−1.46 ± 0.13	2.1	19.1
UCAC4 212-183136	4505±153	1.49 ± 0.36	−1.40 ± 0.13	1.4	4091	4318	4080	0.10	−2.38 ± 0.15	2.7	13.8
UCAC4 308-077592	4210 ± 89	0.60 ± 0.45	−1.67 ± 0.07	1.6	3923	4206	4100	0.60	−1.86 ± 0.13	1.7	6.2
TYC 7262-250-1	4218 ± 73	0.82 ± 0.34	−1.31 ± 0.05	1.6	4193	4121	4217	0.82	−1.36 ± 0.12	1.7	4.3

Note. Also given is the $T_{\rm eff}$ derived from the photometry and listed in the Gaia database. The uncertainties associated with the estimation of stellar parameters in this study are ±150 K for $T_{\rm eff}$, ±0.25 dex for log g, and ±0.15 km s^{-1} for ξ_t.

Table 3
Elemental Abundances of the SLR Stars in This Study

Object Name	A(Li)$_{\rm LTE}$ ± 0.20	A(Li)$_{\rm NLTE}$ ± 0.20	[C/Fe] ± 0.20	[O/Fe] ± 0.20	[Na/Fe] ± 0.20	[Ba/Fe] ± 0.20	[Eu/Fe] ± 0.30
UCAC4 253-045343	3.65	3.60	−0.14	1.03	−0.27	0.56	0.75
UCAC4 099-098976	4.90	4.21	< −0.15	0.96	−0.24	−0.02	< 0.20
UCAC4 212-183136	3.50	3.45	0.08	···	0.58	−0.38	0.86
UCAC4 308-077592	4.45	4.42	−0.03	1.16	−0.24	−0.13	0.45
TYC 7262-250-1	4.38	4.31	−0.19	0.55	−0.05	−0.09	0.59

estimated an error of 150 K on the spectroscopic temperature by ensuring that any alteration in the slope of iron abundances derived from neutral lines with excitation potential remained within 1 s.d. of the Fe I line abundances. The usual technique to derive the surface gravity (log g) assumes ionization equilibrium between Fe I and Fe II lines. Since we have only one clean Fe II line detected in the GALAH spectra, we adopted the log g value when the Fe II abundance was within 1σ of the average Fe I abundances. We assumed an error of 0.25 dex for the estimation of log g. Microturbulent velocity (ξ_t) was calculated by establishing the abundance of Fe I to be independent of reduced EW (log(EW/λ)). An error in the estimation of ξ_t is obtained when the Fe I abundance did not change by more than 1σ and the error is 0.15 km $^{-1}$. The method was iterated until we found a set of $T_{\rm eff}$, log g, and ξ_t values for which we found no significant slope between the abundances of Fe I lines and their LEP values, measured EWs, and the abundances of neutral and ionized lines are equal. The final value of Fe abundance obtained for the converged atmospheric parameters is taken as the metallicity of a star. The derived stellar parameters, the estimated errors in this study, and the values given in the GALAH catalog are listed in Table 2, along with values of $T_{\rm eff}$ derived from the color ($V-K$) and values given in the Gaia catalog. Values of $T_{\rm eff}$ derived here agree very well with the values from Gaia and ($V-K$), but one could notice a significant difference of about 500 K with the GALAH value for the giant UCAC4 212-183136. For the same star, we also found a large difference in log g. However, the log g derived from the Gaia parallax agrees well with our value (see Table 5). The differences between the values derived here and the values given in the GALAH DR3 catalog may be attributed to the choice of model atmospheres, and to some extent, the method of analysis, i.e., pipeline versus manual analysis of star by star. Since the $T_{\rm eff}$ and log g derived here are in good agreement with the values derived from Gaia parallax, we adopt stellar parameters obtained in this study for the abundance analysis.

3.2. Abundances

Due to discrepancies between the stellar parameters from the GALAH data and our values, we reevaluated the abundance of Li and the elements of interest for this study, which include C, O, Na, Ba, and Eu. We used the resonance line at 6707.8 Å to derive the Li abundance and assumed that all the Li present was from the ^{7}Li isotope. The other Li I line, 6103 Å, is not in the spectral range covered by the GALAH survey. We obtained the NLTE corrections for the Li abundances derived by Lind et al. (2009a), and the corrected values are given in Table 3. We also used the 3D NLTE correction code `BREIDABLIK` (Wang et al. 2021) to obtain the 3D NLTE Li abundance. However, the code issued a warning saying that the stellar parameters and LTE Li abundances of all stars in this study are outside the grid utilized in `BREIDABLIK` and the corrections may not be reliable. Nonetheless, according to the grid from Lind et al. (2009a), only the Li abundance in UCAC4 099-098976 falls outside the grid where we performed a linear extrapolation of the grid to obtain the NLTE correction for the star. One can see that the NLTE corrections from Lind et al. (2009a) are very small (∼−0.05) for the cool stars in our sample, whereas for UCAC4 099-098976, which is relatively hotter, the NLTE correction is ∼−0.7 (1D NLTE(A(Li)-1D LTE A(Li))). Such larger corrections have also been reported previously by Li et al. (2018) and Sanna et al. (2020). A higher correction may be needed as the star is relatively hotter and metal-poor in which large overionization takes place. Plots of the best fit with their final abundance values are shown in Figure 2.

The GALAH spectra also cover the spectral features of the O I triplet near 7774 Å, Ba II at 5853.7 Å and 6496.9 Å, and Eu II at 6645.1 Å. Using the spectral synthesis method, we derived the abundances of these elements, and the values are

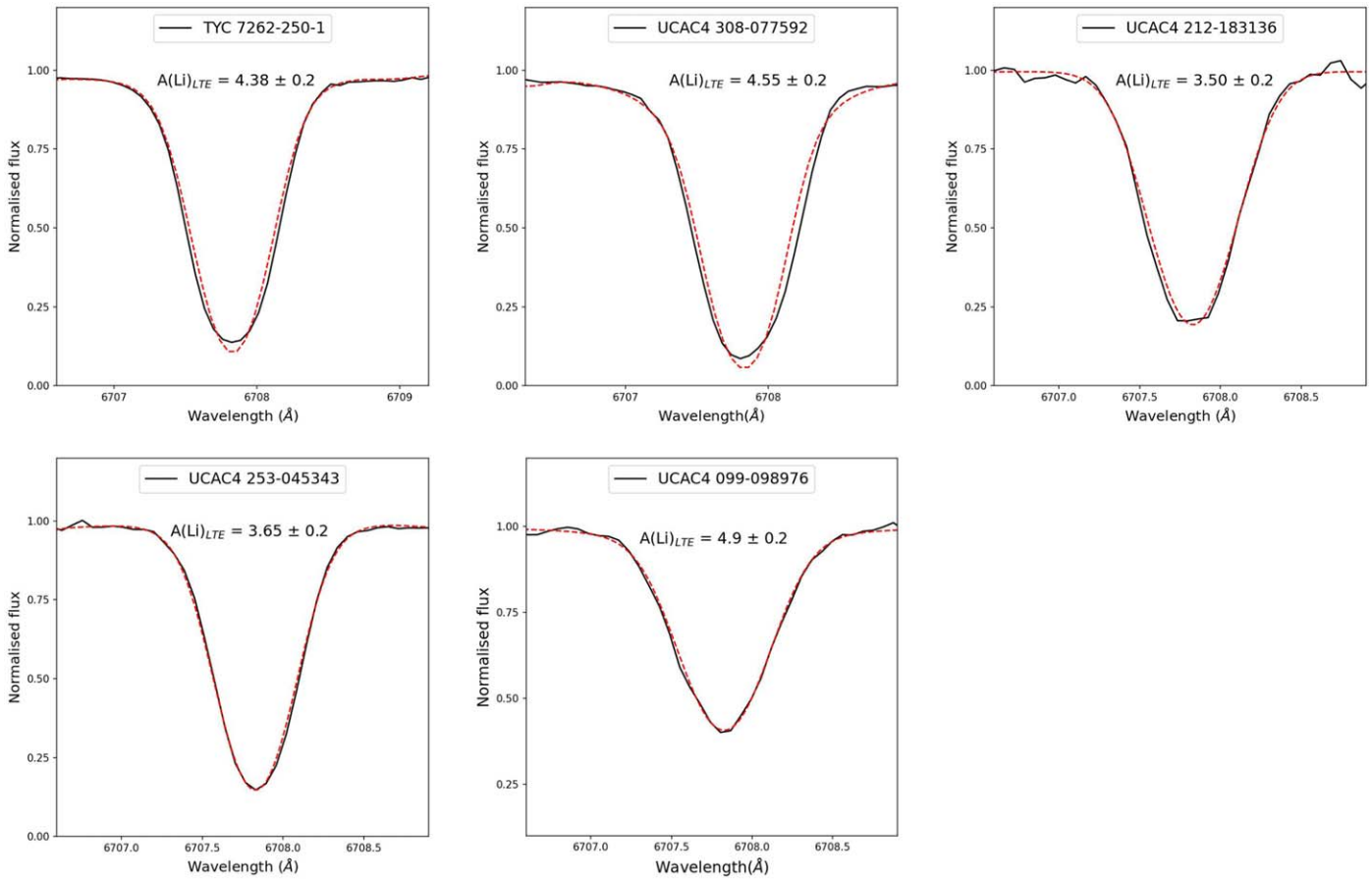

Figure 2. Li line profiles at 6707 Å of the five SLR stars compared with the best-fit synthetic spectra (dashed line).

given in Table 3. To determine the abundance of C, we examined the C_2 molecular bandhead feature at 4737 Å, which was quite weak or absent. Constraining the $^{12}C/^{13}C$ isotopic ratio was particularly challenging, as all our stars are deficient in carbon. Also, the $^{13}C_2$ feature at 4744 Å is too faint to derive the abundance. Additionally, the usual ^{13}CN features (7990–8040 Å) used for deriving the ^{13}C abundance are not covered by the GALAH spectrograph.

All the stars in our sample display depleted C abundance and elevated O abundance. The O abundance was estimated using triplets, but it should be noted that these values have contributions from NLTE effects, and corrections for such effects are not available for cool stars similar to those studied here. Given this limitation, we can only confidently state that oxygen is enhanced. However, providing a quantitative measure of the enhancement after applying the NLTE correction is beyond the scope of this study.

3.2.1. Abundance Errors

The abundances of all the elements except Fe are derived using the spectral synthesis method. So, the uncertainties in the abundance values were estimated through the goodness of the least squares fit, and the values are given in Table 3. For deriving the Fe abundance, we used the method described in Section 3.1. The error due to contributions from uncertainties in EWs and atomic parameters are listed as the 1σ line-to-line scatter, $\sigma_{log\epsilon}$, in Table 2.

4. Other Observed Properties

4.1. H_α Profile and Mass Loss

The profile of the H_α spectral line is an indicator of possible mass loss/stellar activity present in the star and can be detected through asymmetries in the H_α line profile (Mészáros et al. 2009). All five giants show a distorted H_α profile, and three of them also show emission in the H_α wings, as shown in Figure 3. The emissions are also asymmetric. We also examined Ca-triplet features not covered in the GALAH spectra, using Gaia DR3 data (Gaia Collaboration et al. 2023), and the feature seems normal. We looked for possible mass loss using the Two Micron All Sky Survey (2MASS) and Wide-field Infrared Survey Explorer (WISE) all-sky survey of infrared photometry.

The W4-band magnitudes in the WISE catalog have quality flags other than "A." Two of the samples have "U" as the quality flag, which is expected for such fainter sources, as the W4 band has been proven to have very low sensitivity for reliable detection of fainter sources. So we did not calculate the W1–W4 value for those stars, but for the other three stars (UCAC4 253-045343, UCAC4 308-077592, TYC 7262-250-1), we obtained the values for W1−W4 as 0.49, 0.64, and 0.25, respectively. The values are very low, suggesting no active mass loss. None of the giants shows any excess in the infrared colors (J, H, K, and W1, W2, and W3 or W4), suggesting, at least, no hot dust component. We do not have far-IR colors for the sample to check if the stars have cold dust in case the mass loss occurred some time ago.

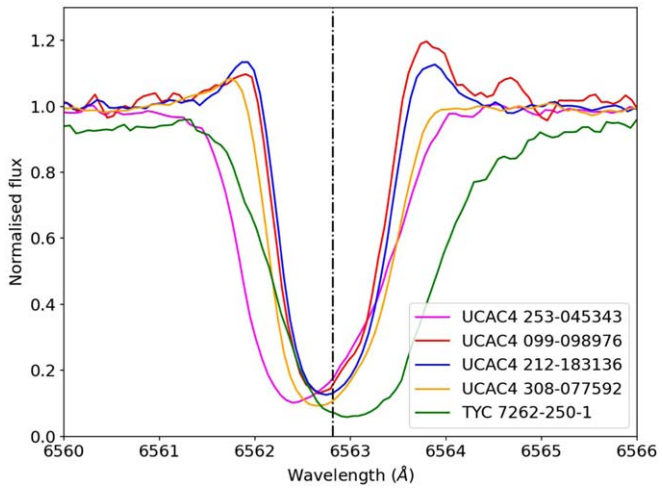

Figure 3. H_α profile of five SLRs. Note that all of them show asymmetry in their profiles.

According to the asymmetric H_α profiles, the emission wings of the H_α line found in metal-poor stars can arise naturally from an extended, static chromosphere (Dupree et al. 1984; Dupree 1986) and may not solely be the signature of mass loss. So, the line asymmetries exhibited by these stars can be attributed to some disturbances in the stellar atmosphere, which would result in local mass flows rather than steady-state mass loss.

4.2. Rotational Velocity

Charbonnel & Lagarde (2010) suggest that the excess Li in some low-mass giants may be due to rotation-induced extra mixing. We derived the giants' projected rotational velocity to see if a correlation exists between Li abundance and the projected rotation velocity, $v \sin i$. GALAH DR3 provided the overall line broadening parameter in the form of *vbroad*, which includes $v \sin i$, and thermal broadening macroturbulence (*vmacro*). We disentangled the *vbroad* into $v \sin i$ and *vmacro* by adopting the relations between *vmacro* and $T_{\rm eff}$ for different luminosity classes according to the recipe given in Hekker & Meléndez (2007). We adopted the method described in Ruchti et al. (2011) to distinguish the luminosity class of each star. Since all the stars except UCAC4 099-098976 lie close to the RGB tip, we classified them as luminosity class II. For UCAC4 099-098976, we used the designation luminosity class III as its location in the H-R diagram is closer to the RGB bump. The derived $v \sin i$ is given in Table 3. According to Carney et al. (2008), the luminous giants with $M_v < -1.5$ exhibit net rotation, and the projected rotation velocity can be larger than 3 km s^{-1}, a typical value for the upper RGB giants.

All the giants in this study show larger $v \sin i$ values than expected, particularly the two giants, UCAC4 099-098976 and UCAC4 212-183136. Fekel & Balachandran (1993) argued that during the convective mixing, redistribution of angular momentum from the dredged-up material could induce increased rotation in stars, creating a dynamo resulting in chromospheric activity. Also, it could be the case where giants show higher rotation due to a sudden decrease in the size, i.e., radius due to He flash and the subsequent transition to the RC phase.

4.3 Radial Velocity

The sample stars' multi-epoch radial velocity (RV) values are important to understanding any RV variation observed. This can be used to distinguish whether any of our giants are a member of a binary system. We examined the RV data from GALAH DR3 and Gaia DR3 (Katz et al. 2023; see Table 1). The RV from Gaia DR3 is obtained by median combining the individual epoch (transit) RVs. The individual epoch radial velocities are not available from Gaia DR3. The RV data from the two catalogs match very well, within 1 km s^{-1}, though they are in two different epochs, indicating no RV variations. We also looked at the renormalized unit weight error (RUWE) of the samples in the Gaia database. The RUWE corresponds to the reduced chi-squared of the best-fitting five-parameter single-body astrometric solution. This error coefficient can be used to identify possible non-single stars, whose RUWE is >1.4 (Lindegren et al. 2018, 2021). All the five giants have an RUWE of <1.4, indicating a lack of binarity. However, for binary systems whose orbital period is larger than about ∼1000 days, the RUWE loses most of its efficiency in detecting binary systems, and RUWE parameters may not provide correct information about their binarity (Jorissen 2019). Hence, even though the RUWE for the samples is < 1.4, the RV variation from a long-period binary companion cannot be ruled out. The kinematic (*U*, *V*, *W*) data provided in the GALAH DR3 catalog suggest that the four giants, including the RC star, belong to the Galactic halo component, whereas TYC 7262-250-1 belongs to the Galactic thick disk (see Table 4).

Table 4
U, V, W Space Velocities of the SLR Stars

Object Name	*U* (km s^{-1})	*V* (km s^{-1})	*W* (km s^{-1})	$V_{\rm total}$ (km s^{-1})
UCAC4 253-045343	−129.2	−173.5	54.2	239.8
UCAC4 099-098976	−186.4	−328.6	−158.1	429.6
UCAC4 212-183136	−46.8	−259.0	−24.4	282.0
UCAC4 308-077592	−74.0	−69.7	−189.2	230.4
TYC 7262-250-1	−45.1	−14.2	104.0	115.7

Note. The last column corresponds to the total space velocity.

5. Evolutionary Phase

It is important to determine the evolutionary phase of Li-rich giants to constrain the origin of Li enhancement. The evolutionary phase could be determined either using the star's location in the H-R diagram combined with the evolutionary tracks or by using asteroseismic data. The latter turned out to be more reliable and is considered the gold standard for separating RC giants of core He burning from those of RGB giants with an inert-He core. Recent studies concluded that SLR giants are most likely to be RC stars rather than RGB stars (Deepak 2019; Singh et al. 2019; Kumar et al. 2020).

5.1. Evolutionary Tracks

GALAH DR3 provides a value-added catalog (VAC) with luminosities calculated using the Bayesian Stellar Parameter Estimation (BSTEP) code from Sharma et al. (2018). BSTEP provides a Bayesian estimate of intrinsic stellar parameters from observed parameters by using the stellar isochrones. Although the luminosities of these stars are readily available from the VAC, due to the change in effective temperature from this study and from the GALAH DR3 catalog (see Table 2), we calculated the luminosity and $\log g$ of these stars using parallaxes obtained from the Gaia DR3 and *V*-band magnitude

Table 5
Luminosity and Log g Derived Using Gaia Parallaxes and V-band Magnitudes[1] of the SLR Stars in This Study

Object Name	A_v (mag)	π (mas)	$\log\left(\frac{L}{L_\odot}\right)$	$\log g$ (dex)
UCAC4 253-045343	0.28	0.13	3.17 ± 0.16	0.75 ± 0.25
UCAC4 099-098976	0.08	0.37	1.73 ± 0.12	2.56 ± 0.16
UCAC4 212-183136	0.09	0.05	3.50 ± 0.22	0.10 ± 0.24
UCAC4 308-077592	0.24	0.05	3.66 ± 0.18	0.33 ± 0.21
TYC 7262-250-1	0.16	0.18	3.18 ± 0.20	0.57 ± 0.23

[1] See Section 5.1.

using the relation

$$-2.5 \log \frac{L}{L_\odot} = M_V + \mathrm{BC}_V(T_{\mathrm{eff}}) - M_{\mathrm{bol}_\odot} \quad (1)$$

and

$$\log g = \log g_\odot + \log \frac{M}{M_\odot} + 4 \log \frac{T_{\mathrm{eff}}}{T_{\mathrm{eff}_\odot}} - \log \frac{L}{L_\odot}, \quad (2)$$

where the absolute magnitude in the V band is calculated by

$$M_V = V + 5 - 5 \log_{10} r - A_V \quad (3)$$

and the temperature-dependent bolometric correction is calculated by

$$\mathrm{BC}_V(T_{\mathrm{eff}}) = a + b \log T_{\mathrm{eff}} + c(\log T_{\mathrm{eff}})^2 + d(\log T_{\mathrm{eff}})^3 \ldots \quad (4)$$

Here, a, b, c, and d are the polynomial coefficients of the model function. Values of these coefficients are taken from Torres (2010). The values of $M_{\mathrm{bol}_\odot} = 4.74$, $\log g_\odot = 4.44$, and $T_{\mathrm{eff}_\odot}$=5772 K are adapted for the Sun. r is the distance to the star (in parsec), and A_V is the interstellar extinction in the V band. We obtained the A_V values from Schlafly & Finkbeiner (2011). We used the T_{eff} derived in this study as the input T_{eff} in the above equation, whereas the mass of the star is obtained from the asteroseismic analysis (refer to Section 5.2). The final values are given in Table 5. Within the estimated uncertainties, the log g values derived from Gaia parallaxes agree well with those from GALAH DR3, except for the giant UCAC4 212-183136. For this star, the log g from GALAH DR3 is more than 1 dex compared to the value derived in this study from the spectra and the Gaia parallax (see Section 3.1).

The luminosity values derived here agree well with the values given in the GALAH DR3 VAC within the estimated uncertainties except for one star, UCAC4 099-098976. The H-R diagram of the data set from GALAH DR3 (See Figure 1) shows a well-defined main sequence, sub-giant, and RGB. Also, one can notice two groups of stars on an RGB; one is identified as the luminosity bump, and the other as an RC or horizontal branch. Of the five giants in our sample, one overlaps with the RC region, and the four seem to be much brighter and closer to the early asymptotic giant branch (AGB).

5.2. Asteroseismic Analysis

Asteroseismology has emerged as a valuable tool in distinguishing core He-burning stars from hydrogen-shell-burning RGBs. The turbulent outer layers of RGBs display stochastically excited oscillations, which could be detected from high-precision time series data of long duration, typically facilitated by space missions such as Kepler (Borucki et al. 2010), CoROT (Michel et al. 2008), and the Transiting Exoplanet Survey Satellite (TESS; Ricker et al. 2015). Two distinct types of oscillations are seen in stars: pressure (p-mode) or acoustic mode, typically observed in the outer envelope of the star, and gravity mode (g-mode), predominantly found in the stellar core. Using the analysis of the oscillations associated with the p- and g-modes in red giants, one can derive two characteristic parameters to distinguish giants with an inert-He core, RGB giants, from those of core He-burning RC giants. The two parameters are a large frequency separation ($\Delta\nu$ of P-modes and the average period spacing (ΔP) of mixed modes arising from coupling between the interior g-mode and the envelope p-mode oscillations.

For our analysis, we made use of data from NASA's TESS from the Mikulski Archive for Space Telescopes (MAST) archive.[2] We systematically removed points from the light curves with a quality flag greater than 0 or NaN flux values to ensure good data quality. Although this resulted in removing some data points, which can impact seismic analysis—the number of such excluded points remained minimal compared to the overall data size. To rectify these sudden jumps in measured flux, we applied corrections using the TESS Asteroseismic Science Operations Center (TASOC) pipeline (Handberg et al. 2021). This pipeline employed a piece-wise cubic Hermite polynomial to interpolate the gaps, ensuring a more continuous and consistent light curve. Finally, all corrected light curves for a single object were stitched together using the lightkurve package (Lightkurve Collaboration et al. 2018). The resultant light curves were converted to periodograms for seismic analysis using the Lomb–Scargle periodogram technique. The power density spectrum (PSD) was subjected to background removal using a log-median filter. The PSD is divided by the estimated background noise to create an S/N spectrum.

We selected a small window in the background-corrected PSD showing clear power excess, and the autocorrelation function (ACF) is computed and integrated over this frequency range. The resulting collapsed ACF exhibits a distinct peak. The frequency value corresponding to the highest value of the collapsed ACF gives ν_{max}. The ACF convolves data with a lagged version of itself, and when oscillation modes overlap each other, spikes are seen in the ACF (see Figure 7 in the Appendix for details). The empirical relation given by Stello et al. (2009) gives a rough estimate of $\Delta\nu$,

$$\Delta\nu = (0.263 \pm 0.009)\nu_{\mathrm{max}}^{(0.772 \pm 0.005)}\ \mu\mathrm{Hz}. \quad (5)$$

Lightkurve identifies the peak of the ACF nearest to this estimate and reports it as $\Delta\nu$. Owing to the shorter baseline time series data provided by TESS, the S/N is comparatively low. Hence, for the detection of significant oscillation peaks, we have used only frequencies corresponding to the standard criterion of S/N $>$ 3–4 (Breger et al. 1993; Li et al. 2019). The same background-corrected PSD is used to identify several consecutive dipole modes and estimate the median period spacing ΔP. The measurement of the ΔP of each star is demonstrated in Figure 4.

[2] https://mast.stsci.edu/portal/Mashup/Clients/Mast/Portal.html

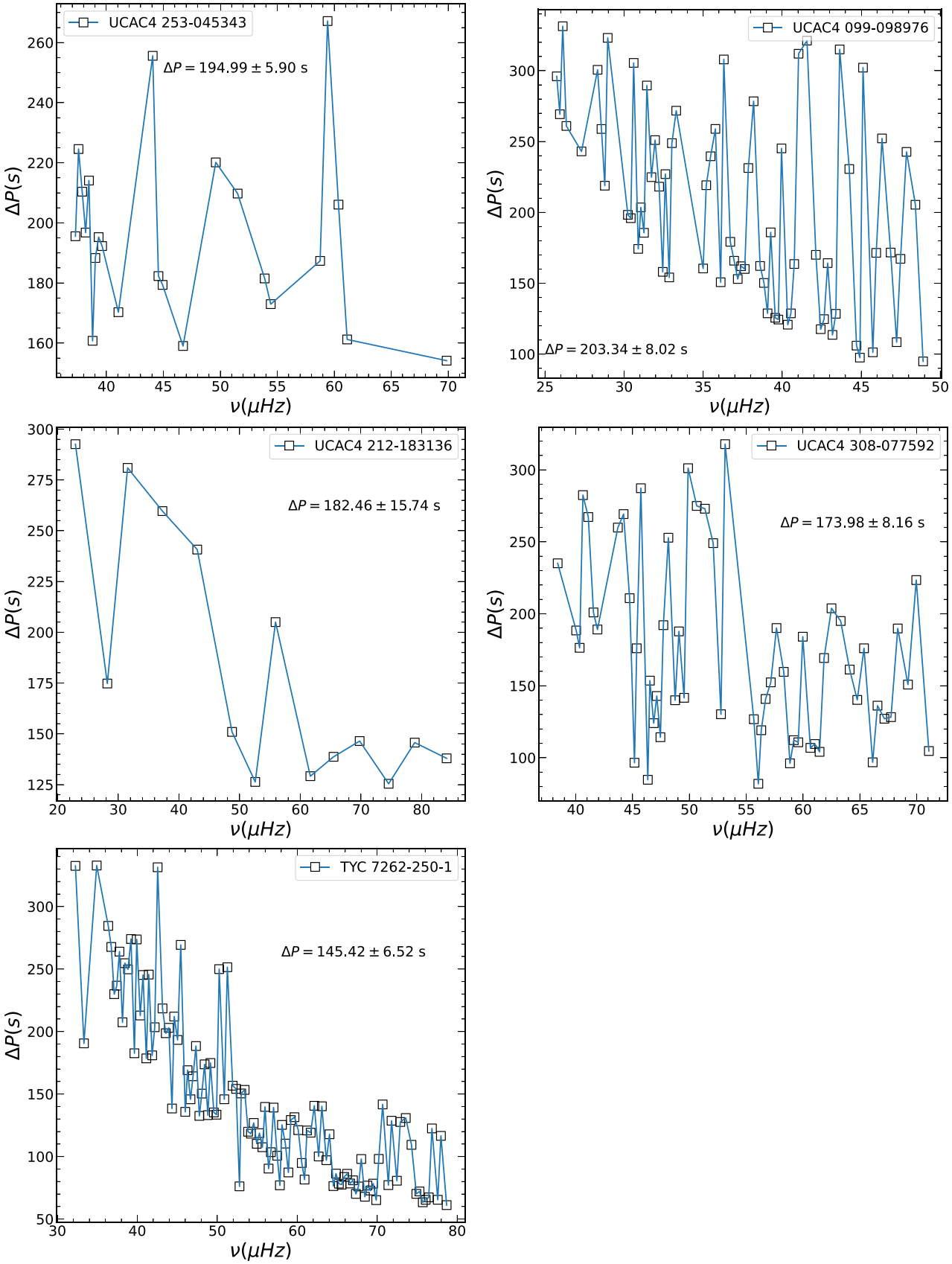

Figure 4. Period spacing measurements for five SLR giants in this study.

Figure 5 shows a ΔP–$\Delta\nu$ diagram of our sample. The RGB stars have a much denser core than core He-burning RC stars. Hence, RC stars exhibit a more pronounced coupling in the mixed modes, which leads to larger ΔP values. Thus, period spacing is a distinctive characteristic that provides a means to distinguish between these distinct phases of stellar evolution

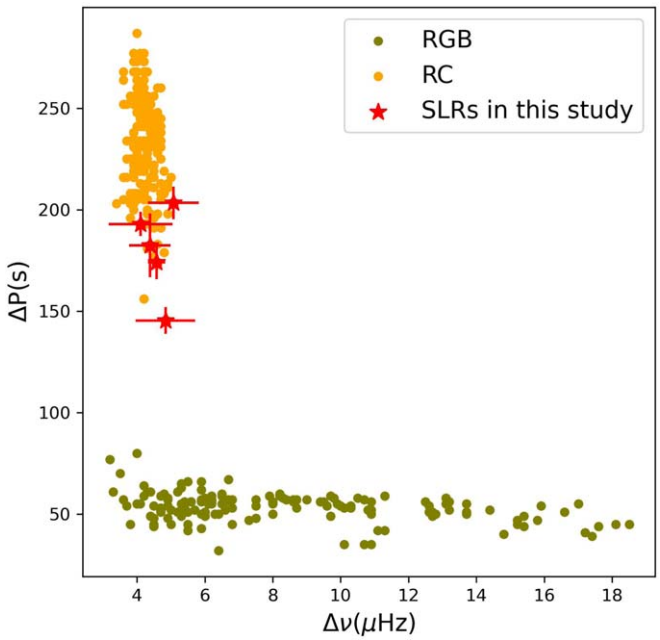

Figure 5. Asteroseismic plot of ΔP–$\Delta\nu$. The dots with respective colors in the background represent stars classified according to evolutionary phases following the classification scheme given in Bedding et al. (2011). RGB stars are marked as olive-colored circles, and RC stars are represented by orange circles. The five SLRs from this study (marked as a red star symbol) show ΔP and $\Delta\nu$ similar to RC stars.

(Bedding et al. 2011). We consider $\Delta P > 100$ s as the RC threshold (Stello et al. 2013). The five giants are shown in the ΔP–$\Delta\nu$ asteroseismic diagram. All five giants fall in the region occupied by giants of the post-He-flash phase, with He burning at the center, and none in the RGB region. Note that Martell et al. (2021) list four of these in their catalog as Li-rich RGB giants using stellar isochrones.

Another significant application of asteroseismology is the determination of fundamental stellar parameters such as mass, radius, and $\log g$. They can be estimated using two seismic scaling relations (Kjeldsen & Bedding 1995):

$$\frac{M}{M_\odot} \approx \left(\frac{\nu_{\rm max}}{\nu_{\rm max,\odot}}\right)^3 \left(\frac{\Delta\nu}{\Delta\nu_\odot}\right)^{-4} \left(\frac{T_{\rm eff}}{T_{\rm eff,\odot}}\right)^{3/2} \quad (6)$$

$$\frac{R}{R_\odot} \approx \left(\frac{\nu_{\rm max}}{\nu_{\rm max,\odot}}\right) \left(\frac{\Delta\nu}{\Delta\nu_\odot}\right)^{-2} \left(\frac{T_{\rm eff}}{T_{\rm eff,\odot}}\right)^{1/2} \quad (7)$$

$$\frac{g}{g_\odot} \approx \left(\frac{\nu_{\rm max}}{\nu_{\rm max,\odot}}\right) \left(\frac{T_{\rm eff}}{T_{\rm eff,\odot}}\right)^{1/2}. \quad (8)$$

From Stefan–Boltzmann law, luminosity can be approximated as

$$\frac{L}{L_\odot} = \left(\frac{R}{R_\odot}\right)^2 \left(\frac{T_{\rm eff}}{T_\odot}\right)^4. \quad (9)$$

The solar reference values are $\nu_{\rm max,\odot} = 3090$ μHz, $\Delta\nu_\odot = 135.1$ μHz (Huber et al. 2010), and $T_{\rm eff,\odot} = 5777.2$ K (Prša et al. 2016) Although scaling relations provide efficient estimation of these parameters, greater accuracy can be achieved through asteroseismic grid modeling. This becomes more pertinent when examining metal-poor stars ([Fe/H] < -1), as scaling relations tend to yield mass estimates that are inflated by roughly 16% (Epstein et al. 2014). In this work, we have used grid modeling to measure mass, radius, and $\log g$. Grid modeling was performed using version 0.0.6 of the ASFGRID code (Sharma et al. 2016; Stello & Sharma 2022). The derived values for all stars are provided in Table 6. The $\log g$ values from the asteroseismic analysis are significantly higher for giants compared to values derived from both the Gaia parallax and in this study, except for one star, which is an RC, where all the methods yield the same $\log g$ or the luminosity.

6. Discussion

The new metal-poor SLRs, along with the known SLRs, are shown in a plot of $\log g$ and $T_{\rm eff}$ (Figure 6, left panel). We have also shown a few metal-rich SLRs (Singh et al. 2021), which have been classified as RC giants using asteroseismic analysis. Two metal-poor SLRs (one from our study and the other from Li et al. 2018) fall in the RC region, and the rest are much brighter, overlapping with the early AGB space in the H-R diagram. We lack asteroseismically determined evolutionary phases for the already known metal-poor SLRs from the literature (see Figure 5). Since all five in this study are in the core He-burning phase, similar to many SLRs in the metal-rich regime, it is reasonable to assume all the known metal-poor SLRs are also in the post-He-flash phase, and none are in the RGB phase. The same sample is shown in the right panel of Figure 6, i.e., in a plot of $\log g$ and A(Li), along with standard model predictions for Li abundances computed using the Modules for Experiments in Stellar Astrophysics (MESA) stellar evolutionary code for $1\,M_\odot$ with two representative values of [Fe/H]. As shown in the figure, Li only gets depleted as giants ascend the RGB, and the value reaches as low as A(Li) $= -2.0$ dex for metal-poor giants upon reaching the RC phase. This implies that the existence of SLRs at evolved phases, either at RC or at the early AGB, does not comply with the existing theoretical models.

The sample SLRs in Figure 6 fall into two distinctive groups: one at the RC near $\log g \sim 2.5$ and the other group at higher luminosity, $\log g \sim 1.0$. According to the metal-rich Li-rich giants at the RC, there are several pieces of evidence showing that Li enrichment occurs during the He flash as the He flash is the only major stellar event before stars arrive on the RC (Singh et al. 2019; Kumar et al. 2020; Singh et al. 2021; Mallick et al. 2023). It is also found that the Li-richness among giants is a transient phenomenon (Singh et al. 2021) as Li starts depleting while they are on the RC, which explains why SLRs are rare. The second group of SLRs at higher luminosity, beyond the RC phase, is interesting. The origin of high Li in these stars is not understood, but their existence suggests multiple mechanisms may be responsible for high Li in giants at different evolutionary phases. Here, we discuss three possibilities for the second group in the H-R diagram.

1. One hypothesis could be that these giants are transitioning to RC post-He ignition at the RGB tip. The location of stars in the H-R diagram and their very high Li abundances do not rule out this possibility. The very high Li and the asteroseismic parameter, the average period spacing (ΔP), imply that these giants have undergone He flash very recently, which has been well demonstrated in the case of metal-rich Li-rich giants (see Singh et al. 2021). If the He flash is the universal origin of high Li in giants, these giants must be in the transition to an RC.

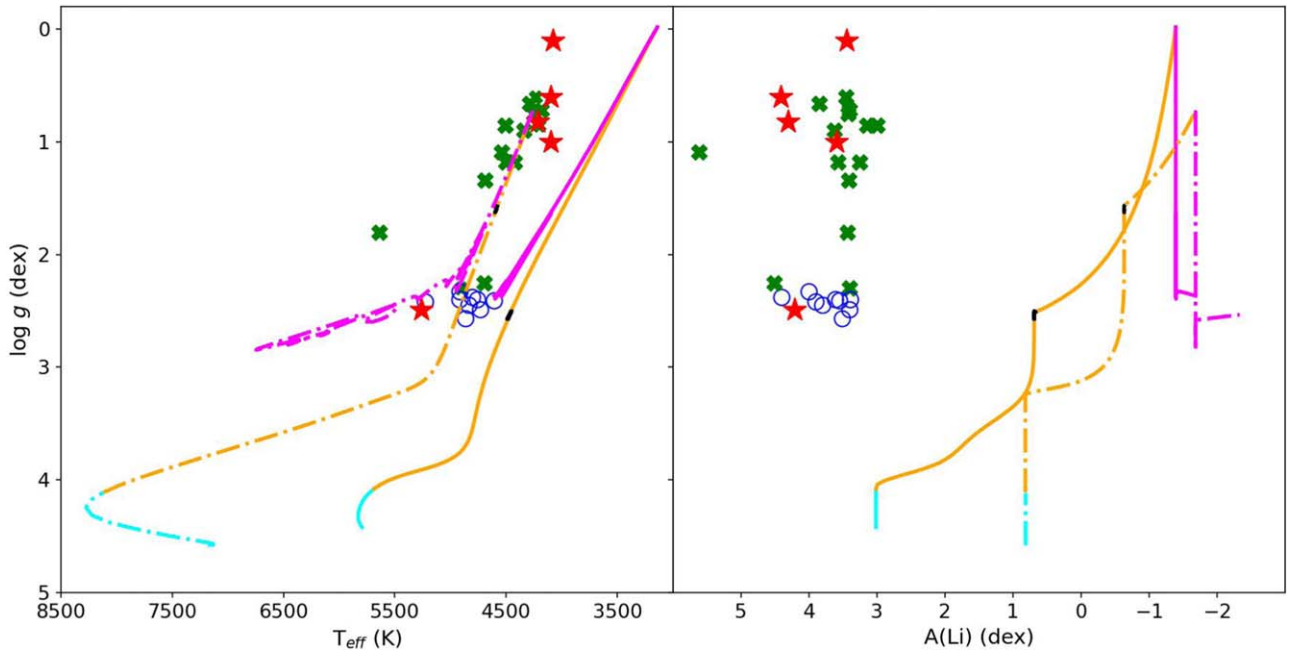

Figure 6. The five metal-poor SLRs in this study (star symbols) are shown in the left panel along with the known metal-poor SLRs (crosses) from Kraft et al. (1999), Ruchti et al. (2011), Kirby et al. (2012), Li et al. (2018), Yan et al. (2018), Sanna et al. (2020) Kowkabany et al. (2022), and Sitnova et al. 2023), metal-rich SLRs (circles) from Singh et al. (2021), and two representative evolutionary tracks for [Fe/H] = −2.5 (dotted–dashed line) and [Fe/H] = 0.0 (continuous line). The color code of the tracks indicates the evolutionary phases: core H burning (cyan), shell H burning (orange), core He burning, (magenta), and RGB luminosity bump (black). In the right panel, the same sample is shown along with the predicted MESA Li evolutionary models for two representative [Fe/H] values. The color code on model tracks is the same as in the left panel.

Table 6
Asteroseismic Parameters of Sample Giants

Object Name	ν_{max} (μHz)	$\Delta\nu$ (μHz)	ΔP (s)	Mass ($M_\odot$)	Radius ($R_\odot$)	log g (dex)	$\log\left(\frac{L}{L_\odot}\right)$
UCAC4 253-045343	36.57 ± 1.09	4.11 ± 0.94	194.99 ± 5.90	1.17 ± 0.53	10.84 ± 3.03	2.44 ± 0.01	1.47 ± 0.28
UCAC4 099-098976	40.62 ± 2.17	5.08 ± 0.75	203.34 ± 8.02	1.04 ± 0.24	9.11 ± 1.38	2.54 ± 0.01	1.76 ± 0.17
UCAC4 212-183136	31.55 ± 1.12	4.38 ± 0.61	182.46 ± 15.74	0.57 ± 0.12	8.14 ± 1.11	2.37 ± 0.01	1.22 ± 0.17
UCAC4 308-077592	45.62 ± 3.39	4.58 ± 0.25	173.98 ± 8.16	1.40 ± 0.04	10.62 ± 0.34	2.53 ± 0.01	1.46 ± 0.09
TYC 7262-250-1	37.99 ± 1.69	4.84 ± 0.88	145.42 ± 6.52	0.72 ± 0.18	8.31 ± 1.33	2.46 ± 0.01	1.29 ± 0.19

Other than these, we do not have any other observable signatures to distinguish a giant, whether it is descending to the RC or evolving off from the RC phase, as the evolutionary paths for a star descending toward RC and ascending toward the early AGB overlap in the H-R diagram.

However, given the timescales involved, the likelihood of finding stars during the transition may be very small. The giants are expected to take about 2 Myr to fully convert the degenerate He core into a convective core He-burning phase of an RC. It is unclear whether the main He flash causes the giants' sudden drop in luminosity to the RC level. If so, we expect the transition period to be about a few hundred days. The subsequent sub-flashes continue in stars at the RC, converting the degenerate core into a fully convective core He burning. Here, we can invoke the analogy of a typical Type 1a supernovae from low-mass stars whose light curves show a drop in brightness by a factor of 10–20 from their peak brightness within about 100 days (Pastorello et al. 2007; Pignata et al. 2008). The only difference is that the star disintegrates in the case of a supernova (SN) explosion, and in the case of He flash, the star is intact except for a sudden drop in the star's luminosity to the RC level, due to a shrink in the star's size. We ran the MESA model of 1 $M_\odot$ with [Fe/H] = −2.5 and examined its evolution from the tip of RGB to the RC. We found that the transient period is about 500 days. Taking an SLR phase of about 2 Myr (see Singh et al. 2021), we find that the probability of finding SLRs during the transition to RC is about one in 2 Myr. In the case of giants, Deepak (2019) found 20 SLRs among the 51,982 RC giants, which is about one in 2500 or a 0.04% probability. However, none were found during the short transition phase from the RGB tip to an RC. On the other hand, in this study, we found four SLRs out of a total sample of 1038 metal-poor giants, i.e., one in 250 giants or 0.4%, which is much larger than the expected probability of detecting SLRs during the transition period or even a factor 10 larger than SLRs among RC giants. The much larger percentage of SLRs among metal-poor giants implies that these four giants may not be in the transition to an RC. The higher percentage of SLR among metal-poor giants also indicates that the SLR phase may last longer among metal-poor giants compared to their counterparts in the metal-rich regime, or

the Li-rich origin among metal-poor giants may differ from that of metal-rich giants.

2. The second possibility is that the giants evolved from the RC phase to an early AGB phase, with a carbon-oxygen core surrounded by He- and H-burning shells. They have probably evolved from an RC, and their high Li abundance may have a different origin other than the He flash. Unfortunately, we do not have asteroseismic signatures for differentiating giants at the RC from those that evolved to the AGB phase. The normal C- and *s*-process elements (see Table 3), signatures of the third dredge-up, indicate that the giants are still at the early AGB phase and have yet to undergo the third dredge-up. It is not clear how these giants became enriched with Li. Is the high Li inherited from the RC or produced in situ at the early AGB phase? Indeed, the high Li cannot be from the RC phase, where most Li produced during the preceding He-flash event might have been destroyed. Singh et al. (2021) demonstrated that Li gets depleted rapidly and set a conservative upper limit of 40 Myr for the SLR phase to last since the ignition of He began at the RGB tip. They argued that since only about 0.3%–0.5% of SLRs are among RC giants, Li must deplete rapidly. Thus, the high Li in the second group may have a different origin other than the He flash. Many studies have argued that the high Li among low-mass giants could be due to cool bottom processing (CBP; Sackmann & Boothroyd 1999; Ruchti et al. 2011) in which additional mixing could occur between radiative layers beneath the deep convective envelope reaching byproducts from H-burning shell. Though the physical mechanism of such a CBP is poorly understood, it has been invoked for high Li seen in low-mass early AGB stars (Abia & Isern 2000).

3. The third possibility is the external origin, like the merger scenario explored by Izzard et al. (2007) and Zhang & Jeffery (2013) to explain high Li among low-mass R- or J-type stars. Zhang & Jeffery (2013) suggest that the merger with He white dwarf (WD) could produce single stars with high Li and similar luminosity to those in the second group. The merger models do not expect enhancement of *s*-process elements and also no enhancement in carbon if the merger involves a red giant and low-mass He WD. Piersanti et al. (2010) conducted a three-dimensional smoothed particle hydrodynamics simulation of a merger between a low-mass He WD and an RGB star, and they identified inefficient He burning, resulting in no carbon enhancement. Zhang & Jeffery (2013) also obtained comparable outcomes from their one-dimensional post-merger calculations using low-mass He WD models. The study by Zhang et al. (2020) of a wide range of progenitor mass binaries revealed that the post-merger abundances are a function of the mass of He WDs. They postulated that Li-rich giants could form from mergers of low-mass He WDs ($0.35\,M_{\odot} \leqslant M_{\rm WD} \leqslant 0.40\,M_{\odot}$) with a low-mass RGB star. Evidence for stellar merger could be the presence of IR excess and dust. Unfortunately, only near-infrared data for these stars in the 2MASS JHK_s bands is available, and their spectral energy distributions exhibit no IR excess. Far-infrared data is essential to confirm IR excess.

Interestingly, we found that luminosity values derived from asteroseismic analysis for the four SLRs are significantly lower than those found from Gaia parallaxes. However, for the RC giant UCAC4 099-098976, the luminosity values derived from both methods are the same (see Tables 5 and 6). We also checked the luminosity values derived from both methods for normal giants with little or no Li at the early AGB phase and found no difference in the luminosity values. It is unclear at this point whether the difference could be due to the merger history of these SLRs. A merger could manifest the giant with higher luminosity, due to increased mass and size. The increased mass may not affect the dense degenerate core at the center; hence, there is little or no change in oscillations from the pre-merger giant. This implies that the four SLRs at higher luminosity probably had a merger history and not the one at the RC. Unfortunately, the absence of TESS/Kepler data hindered our ability to confirm the evolutionary origin of two SLRs studied by Ruchti et al. (2011)—whether they resulted from the evolution of single stars or involved a merger event.

7. Conclusion

In this study, we analyzed photometric, spectroscopic, and asteroseismic data of five super Li-rich giants. Among the five, one star is in the RC phase, whereas the other four lie at higher luminosity near the early AGB. By comparing the existing metal-poor giants, we found two distinct groups of metal-poor SLRs: one at RC luminosity and the other at high luminosity near the early AGB phase. The SLRs at the RC most likely originated from the He flash, similar to metal-rich SLRs. The origin of SLRs at the early AGB phase may be either in situ through CBP or externally merger-induced nucleosynthesis and dredge-up. The significant difference between the luminosity values derived from Gaia parallaxes and the asteroseismology indicates some kind of merger events for the SLRs at higher luminosity values. We also discussed whether these giants are in the transition to the RC, post-He flash, and found it is unlikely as the observed percentage of SLRs among the metal-poor giants is much higher compared to the expected SLRs during the transition or among RC giants.

Being a poorly explored population, large statistically uniform samples are required to better understand the evolutionary phase and production of Li. Metal-poor Li-rich giants are crucial for understanding how metallicity affects the production of Li in giants. Also, it is important to measure other key chemical abundance ratios, such as $^{12}C/^{13}C$ and C/N, to understand the dredge-up process and evolutionary phase.

Acknowledgments

This work made use of the Third Data Release of the GALAH Survey (Buder et al. 2021). The GALAH Survey is based on data acquired through the Australian Astronomical Observatory, under programs A/2013B/13 (the GALAH pilot survey); A/2014A/25, A/2015A/19, A2017A/18 (GALAH survey phase 1); A2018A/18 (open clusters with HERMES); A2019A/1 (hierarchical star formation in Ori OB1); A2019A/15 (GALAH survey phase 2); A/2015B/19, A/2016A/22, A/2016B/10, A/2017B/16, A/2018B/15 (HERMES-TESS program); and A/2015A/3, A/2015B/1, A/2015B/19, A/2016A/22, A/2016B/12, A/2017A/14 (HERMES K2-follow-up program). We acknowledge the traditional owners of the land on which the AAT stands, the Gamilaraay people, and pay our respects to elders past and present. This paper includes data that has been provided by AAO Data Central.[3] All light curves for seismic

[3] https://datacentral.org.au

analysis were obtained from the public data archive at MAST.[4] This research made use of the open-source Python packages Lightkurve[5] (Lightkurve Collaboration et al. 2018) and pySYD[6] (Chontos et al. 2022). This work has also made use of data from the European Space Agency mission Gaia,[7] processed by the Gaia Data Processing and Analysis Consortium (DPAC).[8] Funding for DPAC has been provided by national institutions, in particular, the institutions participating in the Gaia Multilateral Agreement. This research has made use of the SIMBAD database, operated at CDS, Strasbourg, France. (Wenger et al. 2000). This research also has made use of the NLTE data obtained from the INSPECT database version 1.0. [9]

Appendix
Lightkurve Results for the Sample Giants

The results of the Lightkurve analysis of the star UCAC4 253-045343 are discussed here (Figure 7). The left subplot has three panels—the top panel displays the S/N periodogram. The vertical red line indicates $\nu_{\max}$. In the middle panel, we apply a two-dimensional ACF to different segments of the periodogram. In the bottom panel, we present the mean collapsed ACF as a function of the central frequency of each segment. A Gaussian curve (shown in blue) is the smoothened collapsed ACF. The right subplot has two panels—the upper panel displays the frequency region over which ACF is evaluated. In the lower panel, we present the ACF

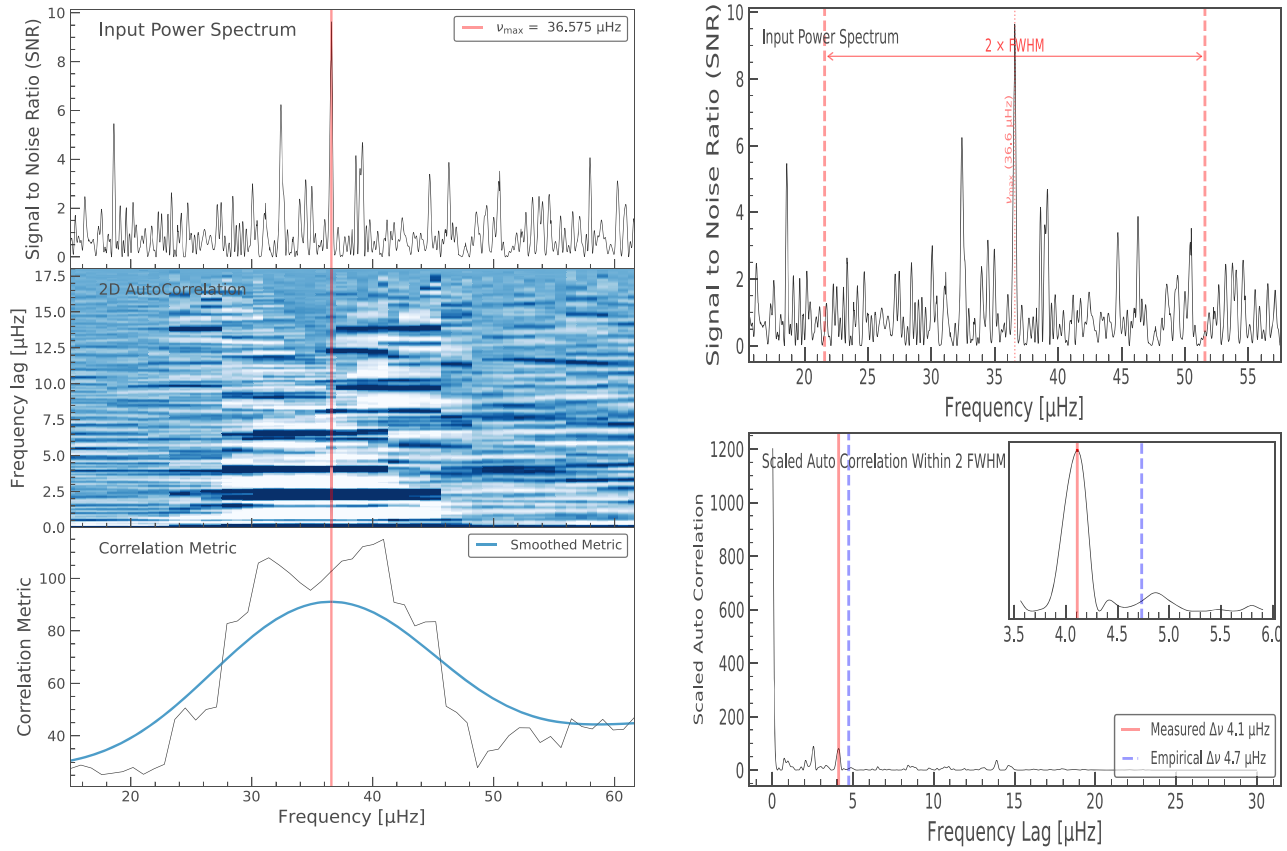

Figure 7. UCAC4 253-045343.

[4] https://mast.stsci.edu/portal/Mashup/Clients/Mast/Portal.html
[5] https://github.com/lightkurve/lightkurve
[6] https://github.com/ashleychontos/pySYD
[7] https://www.cosmos.esa.int/gaia
[8] https://www.cosmos.esa.int/web/gaia/dpac/consortium
[9] http://www.inspect-stars.com/

itself. This is the outcome of computing the correlation between the data and itself while it is progressively shifted over itself.

ORCID iDs

Antony Susmitha https://orcid.org/0000-0002-8519-7353
Anohita Mallick https://orcid.org/0000-0002-4282-605X
Bacham E. Reddy https://orcid.org/0000-0001-9246-9743

References

Abia, C., & Isern, J. 2000, ApJ, 536, 438
Asplund, M., Grevesse, N., Sauval, A. J., & Scott, P. 2009, ARA&A, 47, 481
Battaglia, G., Irwin, M., Tolstoy, E., et al. 2008, MNRAS, 383, 183
Bedding, T. R., Mosser, B., Huber, D., et al. 2011, Natur, 471, 608
Borucki, W. J., Koch, D., Basri, G., et al. 2010, Sci, 327, 977
Breger, M., Stich, J., Garrido, R., et al. 1993, A&A, 271, 482
Buder, S., Sharma, S., Kos, J., et al. 2021, MNRAS, 506, 150
Cameron, A. G. W., & Fowler, W. A. 1971, ApJ, 164, 111
Carney, B. W., Gray, D. F., Yong, D., et al. 2008, AJ, 135, 892
Casey, A. R., Ho, A. Y. Q., Ness, M., et al. 2019, ApJ, 880, 125
Cayrel, G. 1988, in IAU Symp. 132, The Impact of Very High S/N Spectroscopy on Stellar Physics, ed. G. Cayrel de Strobel & M. Spite (Dordrecht: Kluwer)
Charbonnel, C., & Balachandran, S. C. 2000, A&A, 359, 563
Charbonnel, C., & Lagarde, N. 2010, A&A, 522, A10
Chontos, A., Huber, D., Sayeed, M., & Yamsiri, P. 2022, JOSS, 7, 3331
Deepak, Reddy, B. E. 2019, MNRAS, 484, 2000
Denissenkov, P. A., & VandenBerg, D. A. 2003, ApJ, 593, 509
Dupree, A. K. 1986, ARA&A, 24, 377
Dupree, A. K., Hartmann, L., & Avrett, E. H. 1984, ApJL, 281, L37
Epstein, C. R., Elsworth, Y. P., Johnson, J. A., et al. 2014, ApJL, 785, L28
Fekel, F. C., & Balachandran, S. 1993, ApJ, 403, 708
Gaia Collaboration, Vallenari, A., Brown, A. G. A., et al. 2023, A&A, 674, A1
Gratton, R. G., Sneden, C., Carretta, E., & Bragaglia, A. 2000, A&A, 354, 169
Handberg, R., Lund, M. N., White, T. R., et al. 2021, AJ, 162, 170
Hekker, S., & Meléndez, J. 2007, A&A, 475, 1003
Huber, D., Bedding, T. R., Stello, D., et al. 2010, ApJ, 723, 1607
Iben, Icko, J. 1967, ApJ, 147, 624
Izzard, R. G., Jeffery, C. S., & Lattanzio, J. 2007, A&A, 470, 661
Jorissen, A. 2019, MmSAI, 90, 395
Katz, D., Sartoretti, P., Guerrier, A., et al. 2023, A&A, 674, A5
Kirby, E. N., Fu, X., Guhathakurta, P., & Deng, L. 2012, ApJL, 752, L16
Kjeldsen, H., & Bedding, T. R. 1995, A&A, 293, 87
Knauth, D. C., Federman, S. R., & Lambert, D. L. 2003, ApJ, 586, 268
Kowkabany, J., Ezzeddine, R., Charbonnel, C., et al. 2022, arXiv:2209.02184
Kraft, R. P., Peterson, R. C., Guhathakurta, P., et al. 1999, ApJL, 518, L53
Kumar, Y. B., Reddy, B. E., Campbell, S. W., et al. 2020, NatAs, 4, 1059
Kumar, Y. B., Reddy, B. E., & Lambert, D. L. 2011, ApJL, 730, L12
Kupka, F., Piskunov, N., Ryabchikova, T. A., Stempels, H. C., & Weiss, W. W. 1999, A&AS, 138, 119
Lattanzio, J. C., Siess, L., Church, R. P., et al. 2015, MNRAS, 446, 2673
Li, G., Van Reeth, T., Bedding, T. R., Murphy, S. J., & Antoci, V. 2019, MNRAS, 487, 782
Li, H., Aoki, W., Matsuno, T., et al. 2018, ApJL, 852, L31
Lightkurve Collaboration, Cardoso, J. V. D. M., Hedges, C., et al., 2018 Lightkurve: Kepler and TESS time series analysis in Python, Astrophysics Source Code Library, ascl:1812.013
Lind, K., Asplund, M., & Barklem, P. S. 2009a, A&A, 503, 541
Lind, K., Primas, F., Charbonnel, C., Grundahl, F., & Asplund, M. 2009b, A&A, 503, 545
Lindegren, L., Bastian, U., Biermann, M., et al. 2021, A&A, 649, A4
Lindegren, L., Hernández, J., Bombrun, A., et al. 2018, A&A, 616, A2
Luck, R. E. 1982, PASP, 94, 811
Mallick, A., Singh, R., & Reddy, B. E. 2023, ApJL, 944, L5
Martell, S. L., Simpson, J. D., Balasubramaniam, A. G., et al. 2021, MNRAS, 505, 5340
Mészáros, S., Allende Prieto, C., Edvardsson, B., et al. 2012, AJ, 144, 120
Mészáros, S., Dupree, A. K., & Szalai, T. 2009, AJ, 137, 4282
Michel, E., Baglin, A., Weiss, W. W., et al. 2008, CoAst, 156, 73
Mucciarelli, A. 2011, A&A, 528, A44
Pastorello, A., Taubenberger, S., Elias-Rosa, N., et al. 2007, MNRAS, 376, 1301
Piersanti, L., Cabezón, R. M., Zamora, O., et al. 2010, A&A, 522, A80
Pignata, G., Benetti, S., Mazzali, P. A., et al. 2008, MNRAS, 388, 971
Plez, B., 2012 Turbospectrum: Code for spectral synthesis, Astrophysics Source Code Library, ascl:1205.004
Plez, B., & Cohen, J. G. 2005, A&A, 434, 1117
Prša, A., Harmanec, P., Torres, G., et al. 2016, AJ, 152, 41
Ricker, G. R., Winn, J. N., Vanderspek, R., et al. 2015, JATIS, 1, 014003
Ruchti, G. R., Fulbright, J. P., Wyse, R. F. G., et al. 2011, ApJ, 743, 107
Sackmann, I. J., & Boothroyd, A. I. 1999, ApJ, 510, 217
Sanna, N., Franciosini, E., Pancino, E., et al. 2020, A&A, 639, L2
Schlafly, E. F., & Finkbeiner, D. P. 2011, ApJ, 737, 103
Sharma, S., Stello, D., Bland-Hawthorn, J., Huber, D., & Bedding, T. R. 2016, ApJ, 822, 15
Sharma, S., Stello, D., Buder, S., et al. 2018, MNRAS, 473, 2004
Sheinis, A., Anguiano, B., Asplund, M., et al. 2015, JATIS, 1, 035002
Singh, R., Reddy, B. E., Bharat Kumar, Y., & Antia, H. M. 2019, ApJL, 878, L21
Singh, R., Reddy, B. E., Campbell, S. W., Kumar, Y. B., & Vrard, M. 2021, ApJL, 913, L4
Sitnova, T. M., Matsuno, T., Yuan, Z., et al. 2023, MNRAS, 526, 5976
Stello, D., Chaplin, W. J., Basu, S., Elsworth, Y., & Bedding, T. R. 2009, MNRAS, 400, L80
Stello, D., Huber, D., Bedding, T. R., et al. 2013, ApJL, 765, L41
Stello, D., & Sharma, S. 2022, RNAAS, 6, 168
Torres, G. 2010, AJ, 140, 1158
Wallerstein, G., & Sneden, C. 1982, ApJ, 255, 577
Wang, E. X., Nordlander, T., Asplund, M., et al. 2021, MNRAS, 500, 2159
Wenger, M., Ochsenbein, F., Egret, D., et al. 2000, A&AS, 143, 9
Yan, H.-L., Shi, J.-R., Zhou, Y.-T., et al. 2018, NatAs, 2, 790
Zhang, X., & Jeffery, C. S. 2013, MNRAS, 430, 2113
Zhang, X., Jeffery, C. S., Li, Y., & Bi, S. 2020, ApJ, 889, 33